PAPER

Check for updates

Radially evolving spiral wave patterns in the Gierer–Meinhardt reaction–diffusion system†

Tarpan Maiti, [ID] ‡ Achal Jadhav [ID] ‡ and Pushpita Ghosh [ID] *

Spiral wave formation in spatially extended systems is a fascinating phenomenon that has garnered significant attention in reaction–diffusion systems. In this study, we explore the emergence of spiral wave-like patterns in the Gierer–Meinhardt reaction–diffusion model. By employing a multiple-time scale perturbation technique, we derive amplitude equations that reveal the conditions for spiral wave formation. Notably, our analysis shows that the amplitude of these spiral waves varies with the radial distance, introducing a distinctive feature to this pattern. Our theoretical predictions are further substantiated by numerical simulations, which confirm the emergence of spiral wave structures and validate the distinct radial dependence of their amplitude.

1 Introduction

Self-organized pattern formation, one of the most captivating out-of-equilibrium phenomena, has drawn immense attention over recent decades. Beyond biological systems, such phenomena have been observed in a wide variety of chemical and physical systems.[1,2] Alan Turing's pioneering work on reaction–diffusion systems, which proposed diffusion-driven instability in activator–inhibitor kinetics as the fundamental mechanism behind self-organization, has laid the foundation for extensive research in this field.[3,4] This framework has revealed a plethora of spatiotemporal structures, such as stripes, spots, traveling waves, labyrinthine patterns, and others, both experimentally[5–7] and theoretically.[8–10] Among these, spiral wave patterns stand out as a particularly fascinating example of spatiotemporal organization.

A spiral wave is a two-dimensional structure that propagates either outward from or inward toward a central core, forming a characteristic spiral geometry. The Belousov–Zhabotinsky (BZ) reaction, a classical example of a homogeneous reaction–diffusion system, has been widely studied for its ability to generate oscillatory behavior and spatially extended patterns such as spiral and target waves. The first experimental observation of spiral waves was achieved in the Belousov–Zhabotinsky (BZ) reaction,[11–14] followed by similar findings in other chemical systems such as the sodium silicate–cobalt chloride reaction,[15] the photosensitive chlorine dioxide iodine malonic acid reaction.[16] Similarly, heterogeneous autocatalytic

reactions, including the oxidation of CO on platinum surfaces, exhibit rich spatiotemporal dynamics governed by reaction–diffusion mechanisms.[17] Beyond these, precipitating reaction–diffusion systems have also been shown to produce intricate patterns, including Liesegang rings and reaction-driven waves, which share similarities with spiral and target waves observed in classical reaction–diffusion models.[18–21] In electrochemical and metal co-deposition systems, reaction–diffusion dynamics play a crucial role in the formation of complex spatiotemporal structures, including spiral waves and target patterns, influenced by the coupling between reaction kinetics and mass transport.[22–24]

Spiral waves have also been observed in numerous biological processes, including the aggregation of slime molds,[25] the development of frog eggs,[26] cardiac arrhythmias,[27] fertilized starfish eggs,[28] and dense bacterial populations,[29] among others. From a theoretical perspective, various reaction–diffusion models have successfully captured spiral wave dynamics. These include chemical models such as the Oregonator model for the BZ reaction,[30,31] the CDIMA reaction–diffusion model,[8,32,33] and the delayed-feedback induced spiral in Brusselator model.[34] Similarly, biological self-organization processes have been described using models such as the FitzHugh–Nagumo,[35,36] Hastings–Powell,[37] and Decroly–Goldbeter[38] models. The Gierer–Meinhardt (GM) model is another widely studied reaction–diffusion framework, originally developed to elucidate spatial pattern formation during morphogenesis.[39] This model has been instrumental in simulating a range of patterns, including spots, stripes, combinations of spots and stripes,[40–43] as well as traveling wave-like patterns.[44] However, the dynamics of spiral waves within the GM model remain underexplored, particularly from a numerical analysis perspective. Bhattacharyay *et al.*[45] analytically demonstrated the potential for spiral and target wave formation in the GM system

School of Chemistry, IISER Thiruvananthapuram, Kerala 695551, India. E-mail: pushpita@iisertvm.ac.in

‡ These authors contributed equally to this work.

using multiple-scale analysis. However, numerical validation of these insights is lacking, highlighting the need for further investigation. These diverse systems highlight the universality of RD-driven pattern formation and motivate further investigation into the underlying mechanisms that govern the emergence of novel structures. Understanding the conditions under which these patterns arise, particularly the variation of spiral wave amplitudes or frequency modulation, has broad implications for nonlinear chemical dynamics, biological morphogenesis, and materials science.

In this study, we undertake a comprehensive exploration of spiral wave dynamics in the GM reaction–diffusion system from both analytical and numerical perspectives. Employing the multiple-scale analysis technique,[45–48] a weakly nonlinear analysis, we derive amplitude equations to elucidate the conditions for spiral wave formation. To corroborate these analytical findings, we perform numerical simulations and examine the emergence of spiral waves under both zero-flux and periodic boundary conditions. Furthermore, we investigate the dependence of spiral wave formation on domain size and grid resolution, to ensure the robustness of the spiral waves providing deeper insights into the system's behavior. Remarkably, our findings reveal the existence of amplitude variations of the developed spiral waves in GM model, radially-varying spiral wave patterns, a phenomenon not previously reported to the best of our knowledge. The derived amplitude equations predict this unique behavior, offering valuable insights into the radially-evolving spiral wave dynamics in the GM model. This distinctive characteristic sets our study apart from existing research on spiral wave dynamics and highlights the novel contributions of our work. Understanding the variation of spiral wave amplitudes in reaction–diffusion (RD) systems is essential for advancing multiple scientific fields. In nonlinear chemical dynamics, such variations reveal instabilities and mode selection, refining models of self-organization in chemical systems. In biological morphogenesis, they influence processes like cell signaling, cardiac waves, and tissue development, with implications for disease modeling. In materials science, amplitude variations impact pattern formation in electrochemical and metal co-deposition systems, affecting surface morphology, nanoscale fabrication, and corrosion control. Similarly, in precipitating RD systems, they offer pathways for designing ordered material structures with specific functionalities.

2 The model

In this study, we consider the two-variable Gierer–Meinhardt (GM) model,[39,40] which was originally proposed to describe the emergence of spatial patterns in tissue structures, starting from nearly homogeneous conditions during embryological development and regeneration. The model builds upon Alan Turing's groundbreaking concept of reaction–diffusion systems, specifically emphasizing the autocatalytic behavior of an activator and the cross-catalytic inhibition mediated by an inhibitor. The governing equations of the original two-variable GM model are given as follows:

$$\frac{\partial U}{\partial T} = \rho_U \frac{U^2}{(1 + k_U U^2) V} - \mu_U U + \sigma_U + D_U \nabla^2 U, \quad (1a)$$

$$\frac{\partial V}{\partial T} = \rho_V U^2 - \mu_V V + \sigma_V + D_V \nabla^2 V. \quad (1b)$$

Here, U and V represent the concentration of the activator and inhibitor species, respectively, and thus have the dimension of concentration. In accordance with the activator–inhibitor dynamics of a reaction–diffusion system, the activator species promotes the production of both itself and the inhibitor, while the inhibitor suppresses the activator's production. The term $\left(\frac{U^2}{1 + k_U U^2}\right)$ captures the saturable nature of activator production, with k_U serving as the saturation constant. The parameters σ_U and σ_V are the basic production term of the activator and inhibitor, respectively, while the removal rates of the two species are represented by μ_U, μ_V. ρ_U and ρ_V are the cross-reaction coefficients and are related to the product of the rate constant and source densities of the activator and inhibitor species, respectively. The diffusion coefficients for the activator and inhibitor are denoted by D_U and D_V. Although this model was originally proposed to explain the development of spatial patterns in tissue structures during morphogenesis, it can also describe spatiotemporal pattern formation observed in various chemical systems. To reduce the complexity of the equation, we set the saturation constant (k_U) and the basic production term of the inhibitor (σ_V) to zero in the current investigation.[40] This scenario closely resembles a chemical reaction occurring in a continuously stirred tank reactor (CSTR),[49] where reactants and products are continuously introduced and removed. During these reactions, intermediate species[50] generated in the system act as activator and inhibitor components. The following dimensionless quantities have been introduced to render the overall eqn (1) dimensionless:

$$t = \mu_U T, \quad x = \sqrt{\frac{\mu_U}{D_V}} X, \quad y = \sqrt{\frac{\mu_U}{D_V}} Y, \quad u = \frac{\mu_U \rho_V}{\mu_V \rho_U} U,$$

$$v = \frac{\mu_U^2 \rho_V}{\mu_V \rho_U^2} V.$$

Substituting these transformations, eqn (1) becomes:

$$\frac{\partial u}{\partial t} = \left(\frac{u^2}{v} - u + \sigma\right) + D \nabla^2 u, \quad (2a)$$

$$\frac{\partial v}{\partial t} = \mu(u^2 - v) + \nabla^2 v. \quad (2b)$$

Here, $D = \frac{D_U}{D_V}$, $\mu = \frac{\mu_V}{\mu_U}$, and $\sigma = \frac{\rho_V \sigma_U}{\mu_V \rho_U}$ are dimensionless parameters. Setting the reaction terms in eqn (2) to zero provides the system's homogeneous steady state, given by $(u_{ss}, v_{ss}) = [(1 + \sigma), (1 + \sigma)^2]$.

2.1 Linear stability analysis: Hopf and Turing instability

We performed a systematic linear stability analysis around the homogeneous steady state of the system in the absence of
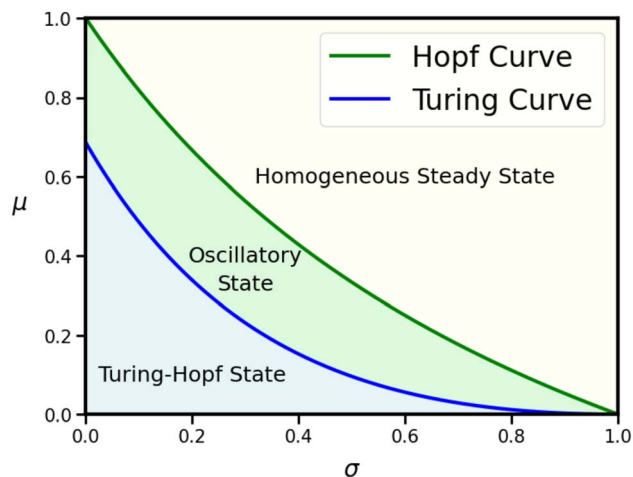
Fig. 1 Bifurcation diagram obtained from linear stability analysis of eqn (2) of the GM model for the parameter values: $D = 0.25$. The region above and below the Hopf curve (green line) represents temporally stable and unstable regions, respectively. The region above and below the Turing curve (blue line) represents spatially stable and unstable regions, respectively.

diffusion. This analysis provides the condition for Hopf bifurcation in the parameter space as $\mu_H = \dfrac{1-\sigma}{1+\sigma}$. The Hopf bifurcation curve separates the parameter space into regions of temporally stable and unstable states. Subsequently, we carried out the stability analysis of the spatially extended GM model around the homogeneous steady state in the presence of diffusion. This yields the Turing condition as: $\mu_T = \dfrac{1}{D}\left(\sqrt{\dfrac{2}{1+\sigma}}-1\right)$. The Turing curve divides the parameter space into two regions, indicating the presence of diffusion-driven instability. Fig. 1 illustrates the corresponding bifurcation diagram for a fixed value of $D = 0.25$ in the μ vs. σ parameter space. The three distinct regions, marked with different colors, represent the relevant spatiotemporal instabilities identified through linear stability analysis. Based on prior literature,[48] the oscillatory region near the Turing curve will be our primary focus for spiral wave formation.

3 Derivation of amplitude equation for spiral waves: a multiple timescale based analysis

To explore the existence of spiral wave solutions in the spatially extended system, we employ the well-established multiple-scale perturbation technique, as mentioned earlier. The multiple time-scale perturbation method is a well-established technique within the broader framework of weakly nonlinear analysis (WNL). It has been successfully applied to predict the emergence of target and spiral waves, as well as other spatiotemporal instabilities, in various reaction–diffusion systems, including biological morphogenesis,[45] the chlorine dioxide–iodine–malonic acid system,[46,47] and prey-predator models.[48,51] This method allows for the systematic derivation of amplitude

equations governing spiral wave formation near the bifurcation. Additionally, other weakly nonlinear analysis techniques have been effectively used to study the emergence of spiral waves, Turing patterns, and other spatiotemporal structures in electrochemical and metal co-deposition systems.[23,52] The general reaction–diffusion equations for the Gierer–Meinhardt (GM) model, as described in Section 2, are given by:

$$\frac{\partial u(x,y,t)}{\partial t} = f(u,v) + D\nabla^2 u \tag{3a}$$

$$\frac{\partial v(x,y,t)}{\partial t} = \mu g(u,v) + \nabla^2 v \tag{3b}$$

Here, μ serves as our control bifurcation parameter, determining how far we can move from the Hopf curve to achieve the spiral wave-like structure. As done earlier when deriving the Hopf and Turing conditions, we introduce a small perturbation $[\delta u(x,y,t),\ \delta v(x,y,t)]$ around the system's homogeneous steady state (u_{ss}, v_{ss}). The key distinction in this instance lies in how this small perturbation is expressed, which will now follow the framework of multiple scales. Performing a Taylor series expansion of the reaction terms and neglecting higher-order terms, eqn (3) reduces to the following linearized form:

$$\frac{\partial(\delta u)}{\partial t} = f_u(\delta u) + f_v(\delta v) + D\nabla^2 u \tag{4a}$$

$$\frac{\partial(\delta v)}{\partial t} = \mu g_u(\delta u) + \mu g_v(\delta v) + \nabla^2 v \tag{4b}$$

where f_u, f_v, g_u, and g_v are the partial derivatives of the reaction terms with respect to u and v, evaluated at the steady state.

We expand the control parameter μ around the Hopf bifurcation point (μ_0) as $\mu = \mu_0 + \varepsilon\mu_1$, where $0 < \varepsilon < 1$. The choice of ε is not unique, so our focus will be on deriving the expression for $\varepsilon\mu_1$ as a whole. This provides valuable information regarding how far from the Hopf curve the spiral solution can be observed. Given the intrinsic spiral nature of the solution, it is advantageous to work in polar coordinates. Thus, we scale the spatial coordinates in two dimensions (polar coordinates) as $\theta = \varepsilon^{1/2}\theta_1$ and $r = r_0 + \varepsilon r_1$. Similarly, the time variable is written as $t = t_0 + \varepsilon\tau$. The perturbations $(\delta u, \delta v)$ are expanded in the following form:

$$\delta u = \varepsilon u_1 + \varepsilon^2 u_2 + \ldots \tag{5a}$$

$$\delta v = \varepsilon v_1 + \varepsilon^2 v_2 + \ldots \tag{5b}$$

Substituting these expressions into eqn (4) we get:

$$\varepsilon\left(\frac{\partial u_1}{\partial t_0} - f_u u_1 - f_v v_1 - D\nabla_0^2 u_1\right)$$
$$+ \varepsilon^2\left(\frac{\partial u_2}{\partial t_0} + \frac{\partial u_1}{\partial \tau} - f_u u_2 - f_v v_2 - D\nabla_0^2 u_2 - D\nabla_\varepsilon^2 u_1\right) + \ldots = 0 \tag{6}$$

$$\varepsilon\left(\frac{\partial v_1}{\partial t_0} - \mu_0 g_u u_1 - \mu_0 g_v v_1 - \nabla_0^2 v_1\right)$$
$$+ \varepsilon^2\left(\frac{\partial v_2}{\partial t_0} + \frac{\partial v_1}{\partial \tau} - \mu_0 g_u u_2 - \mu_0 g_v v_2 - \mu_1 g_u u_1 - \mu_1 g_v v_1 - \right.$$
$$\left. \nabla_0^2 v_2 - \nabla_\varepsilon^2 v_1\right) + \ldots = 0 \tag{7}$$

where,

$$\nabla_0{}^2 = \frac{1}{r_0}\frac{\partial}{\partial r_0}r_0\frac{\partial}{\partial r_0} + \frac{1}{r_0{}^2}\frac{\partial^2}{\partial \theta^2}$$

$$\nabla_\varepsilon{}^2 = \frac{1}{r_0}\frac{\partial}{\partial r_0}r_0\frac{\partial}{\partial r_1} + \frac{1}{r_0{}^2}\frac{\partial^2}{\partial \theta^2}$$

Next, we collect the coefficients of $O(\varepsilon)$ from both sides of eqn (6) and (7), yielding the following equations:

$$\begin{pmatrix} \frac{\partial}{\partial t_0} - D\nabla_0{}^2 - f_u & -f_v \\ -\mu_0 g_u & \frac{\partial}{\partial t_0} - \nabla_0{}^2 - \mu_0 g_v \end{pmatrix}\begin{pmatrix} u_1 \\ v_1 \end{pmatrix} = \hat{L}\begin{pmatrix} u_1 \\ v_1 \end{pmatrix} = 0 \tag{8}$$

Now, since the spirals are observed near the Hopf bifurcation threshold, we assume the trial solution (u_1, v_1) to take the following form:

$$\begin{pmatrix} u_1 \\ v_1 \end{pmatrix} = A(r_1, \theta_1, \tau)\begin{pmatrix} \bar{u}_1 \\ \bar{v}_1 \end{pmatrix}e^{\gamma t_0} \tag{9}$$

where $A(r_1, \theta_1, \tau)$ is the amplitude function, and $(\bar{u}_1, \bar{v}_1)$ are the eigenvectors corresponding to the eigenvalue γ. The eigenvalue (γ) can be obtained by solving eqn (8) in the absence of the diffusion terms. The corresponding solution for γ is given as:

$$\gamma_{1,2} = \frac{1}{2}\left[(f_u + \mu_0 g_v) \pm \sqrt{(f_u + \mu_0 g_v)^2 - 4\mu_0(f_u g_v - g_u f_v)}\right]. \tag{10}$$

From this equation, we may infer that when $(f_u + \mu_0 g_v) > 0$, the growth rate γ will increase. This condition allows us to determine the Hopf curve as:

$$\mu_0 = -\frac{f_u}{g_v}. \tag{11}$$

This result is consistent with our earlier expression for the Hopf curve. Additionally, we obtain the Hopf frequency as:

$$\omega_H = \sqrt{\mu_0(f_u g_v - g_u f_v)}. \tag{12}$$

Furthermore, substituting the trial solution eqn (9) into eqn (8), we can explicitly solve for $\bar{u}_1$ and $\bar{v}_1$. Consequently, the explicit form of the trial solution becomes:

$$\begin{pmatrix} u_1 \\ v_1 \end{pmatrix} = A(r_1, \theta_1, \tau)\begin{pmatrix} \gamma - \mu_0 g_v \\ \mu_0 g_u \end{pmatrix}e^{\gamma t_0} \tag{13}$$

Next, we seek the higher-order terms, $O(\varepsilon^2)$. As before, we compare the coefficients of ε^2 from both sides of the governing equations. This yields the following set of equations:

$$\hat{L}\begin{pmatrix} u_2 \\ v_2 \end{pmatrix} = \begin{pmatrix} -\frac{\partial}{\partial \tau} + D\nabla_\varepsilon{}^2 & 0 \\ \mu_1 g_u & -\frac{\partial}{\partial \tau} + \nabla_\varepsilon{}^2 + \mu_1 g_v \end{pmatrix}\begin{pmatrix} u_1 \\ v_1 \end{pmatrix} \tag{14}$$

The operator $\hat{L}$ acts on u_1 and v_1 in eqn (8), leading to zero eigenvalues. However, in eqn (14), a non-trivial term arises on the right-hand side due to the action of the operator $\hat{L}$ on u_2 and v_2. Therefore, the solvability criterion (Fredholm theorem) must be applied. According to this condition, the right-hand side of eqn (14) must be orthogonal to the left eigenvector of $\hat{L}$ corresponding to the zero eigenvalue. This condition ultimately leads to the following equation:

$$\begin{pmatrix} u_1^* & v_1^* \end{pmatrix}\begin{pmatrix} -\frac{\partial}{\partial \tau} + D\nabla_\varepsilon{}^2 & 0 \\ \mu_1 g_u & -\frac{\partial}{\partial \tau} + \nabla_\varepsilon{}^2 + \mu_1 g_v \end{pmatrix}\begin{pmatrix} u_1 \\ v_1 \end{pmatrix} = 0 \tag{15}$$

where, u_1^* and v_1^* are the complex conjugate of u_1 and v_1, respectively. Expanding eqn (15) leads to the following equation:

$$-u_1^*\frac{\partial u_1}{\partial \tau} + Du_1^*\nabla_\varepsilon{}^2 u_1 + \mu_1 g_u v_1^* u_1 - v_1^*\frac{\partial v_1}{\partial \tau} + v_1^*\nabla_\varepsilon{}^2 v_1 + \mu_1 g_v v_1^* v_1 = 0 \tag{16}$$

Since the amplitude (A) depends on r_1, θ_1, and t, we revert to the original scale. Ultimately, we obtain the dynamics of the amplitude as follows:

$$\frac{\partial A}{\partial t} = C_1\frac{1}{r}\frac{\partial A}{\partial r} + C_1\frac{1}{r^2}\frac{\partial^2 A}{\partial \theta^2} + i\varepsilon\mu_1 C_2 A \tag{17}$$

Here,

$$C_1 = \frac{D\left[\gamma^2 + (\mu_0 g_v)^2\right] + (\mu_0 g_u)^2}{|\gamma|^2 + (\mu_0 g_u)^2 + (\mu_0 g_v)^2},$$

$$C_2 = \frac{\omega_H \mu_0 g_u{}^2}{|\gamma|^2 + (\mu_0 g_u)^2 + (\mu_0 g_v)^2}$$

To solve eqn (17), we assume a generic solution for the spiral wave[53,54] of the form:

$$A(r, \theta, t) = \bar{A}(r)e^{\eta t}e^{i(\omega t + \psi(r) + m\theta)} \tag{18}$$

where $\bar{A}(r)$ is the amplitude of the spiral, η is the growth rate of the spiral, ω is the angular frequency, $\psi(r)$ determines the type of spiral, and m is the number of arms on the spiral. The sign of m governs the direction of rotation: $m = +1$ for an anticlockwise spiral wave rotating clockwise, and $m = -1$ for a clockwise spiral wave rotating counterclockwise.

Substituting eqn (18) into eqn (17) and comparing the real and imaginary components, we obtain:

$$\eta = \frac{C_1}{r\bar{A}(r)}\frac{\partial \bar{A}(r)}{\partial r} - \frac{C_1}{r^2}m^2 \tag{19}$$

$$\omega = \frac{C_1}{r}\frac{\partial\psi(r)}{\partial r} + \varepsilon\mu_1 C_2 \tag{20}$$

It follows from eqn (19) that if the amplitude ($A(r)$) varies with respect to r, there is a possibility that the spiral's growth rate (η) will be positive. Our analysis predicts the formation of spiral waves with varying amplitude, a feature that aligns with the general predictions of WNL theory. However, while our approach confirms the existence of amplitude variations, it does not fully resolve the nature of the amplitude evolution in space and time. Nonetheless, our results demonstrate that if a spiral wave forms, it will inherently exhibit a radially varying amplitude. Additionally, a spiral with a nonzero frequency requires that eqn (20) be satisfied. Assuming that the spiral type does not change significantly with respect to r, then we can approximate $\frac{\partial\psi(r)}{\partial r} \approx 0$. In this case, eqn (20) can be simplified and expressed as:

$$\varepsilon\mu_1 = \frac{\omega\left[|\gamma|^2 + (\mu_0 g_u)^2 + (\mu_0 g_v)^2\right]}{\omega_H \mu_0 g_u^2} \tag{21}$$

Finally, we can infer that, in addition to the spiral's amplitude fluctuating with r, if eqn (21) is satisfied, a fully developed spiral wave can be observed. Since ω_H represents the Hopf frequency of homogeneous oscillation in this case, we can consider it as a zero-order approximation of the spiral's natural frequency ω. Consequently, ω_H can be equated to ω within a numerical factor ζ, such that $\omega = \zeta\omega_H$. Using this relation, eqn (21) can be written as:

$$\varepsilon\mu_1 = \frac{\zeta\left[|\gamma|^2 + (\mu_0 g_u)^2 + (\mu_0 g_v)^2\right]}{\mu_0 g_u^2} \tag{22}$$

To compare with the numerical findings, we must now determine the value of eqn (22). The only unknown term is ζ. First, we use the formula $(\mu - \mu_0)$ to determine the value of $\varepsilon\mu_1$ numerically. Where μ_0 is the Hopf curve $\left(-\frac{f_u}{g_v}\right)$ and μ is the numerical value at which the first spiral arises. Once we have the value of $\varepsilon\mu_1$ eqn (22) allows us to determine the value of ζ using this value along with the other parameters. Keeping ζ constant for the rest of the parameter set, we can then compare the value of $\varepsilon\mu_1$ value obtained from eqn (22) with the numerical simulations.

4 Numerical analysis

We conducted detailed numerical simulations of eqn (2a) and (2b) for parameter values within the oscillatory region near the Turing curve, as shown in Fig. 1. The explicit Euler method was used for numerical integration, with spatial and temporal discretization. The simulations were performed on a finite system of size $L_x = L_y = 200$ with a grid size of $\delta_x = \delta_y = 1$ and a time step of $dt = 0.001$. A zero-flux boundary condition was applied
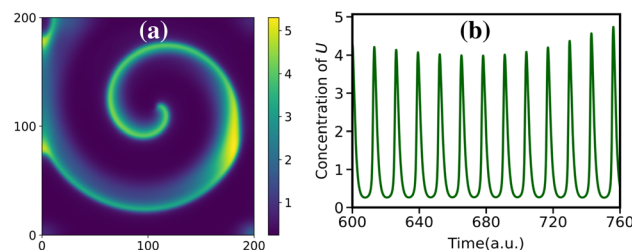

Fig. 2 (a) Numerically simulated concentration profile for the activator concentration (u) obtained by solving eqn (2a) and (2b) shows the emergence of a spiral wave-like structure for the parameter values $D = 0.25$, $\mu = 0.37$, and $\sigma = 0.2$. Domain size of the square box (200×200), grid spacing ($\delta_x = \delta_y$) = 1.0, time step (dt) = 0.001. In the colorbar, the dark blue region represents a low concentration value, while the yellow region demonstrates a high concentration. (b) The corresponding time profile for a fixed point of (100, 100) of (a). Temporal frequency of oscillation is found to be ≈ 0.0765.

throughout the simulations unless otherwise specified. To initiate the dynamics, the system was perturbed at the center of the domain (10×10 mesh) by introducing $\pm 1\%$ random noise around the homogeneous steady state, ensuring the breaking of spatial symmetry. Numerical simulations confirm the feasibility of obtaining spiral waves in the system. Fig. 2(a) shows the concentration profile of the activator (u) for the parameter values $D = 0.25$, $\sigma = 0.2$, and $\mu = 0.37$. The corresponding time evolution of the activator concentration at a fixed point (100, 100) is presented in Fig. 2(b), from which the spiral's frequency was determined to be ≈ 0.0765. A detailed video representation, available in SM (Movie 1), illustrates the observed spiral's temporal dynamics-rotating inwardly in an anticlockwise direction while spatially exhibiting a clockwise geometry.

A closer examination of the spiral wave pattern reveals that its amplitude is not constant with respect to the radial distance r. Notably, one of the insights derived from the analytical investigation suggests that the spiral's amplitude must vary with r for it to grow. To better visualize this behavior, Fig. 3(a) provides a contour diagram of the activator concentration (u), highlighting regions where amplitude changes are most prominent. To further elucidate, Fig. 3(b) displays heatmaps of the spiral arm's concentration profile for two specific regions, A and B, marked by blue arrows in Fig. 3(a), extending from the spiral perimeter toward the core. The differing color intensities between regions A and B indicate a clear variation in the spiral's amplitude with respect to r, corroborating the analytical predictions. Interestingly, there are only a few documented instances where the amplitude of spiral waves varies with respect to the radial distance r. Elmegreen et al.[55] observed variations in spiral arm amplitude in the grand design galaxies M51, M81, and M100. Beyond amplitude fluctuations, Li et al.[56] demonstrated the formation of dense-sparse and sparse-dense spiral waves in complex Ginzburg–Landau reaction–diffusion systems, where the breadth of the spiral arm changes with r. As far as reaction–diffusion systems are concerned, our study is the first to demonstrate the emergence of spirals with variable amplitude with respect to r.
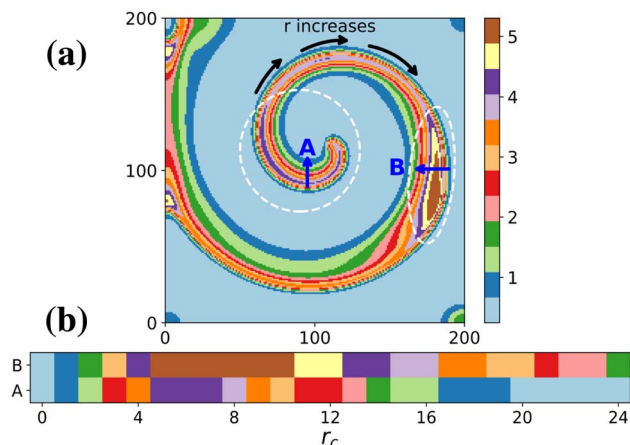
Fig. 3 (a) Colored contour diagram of spiral wave for the activator concentration (u) for the parameter values $D = 0.25$, $\mu = 0.37$, and $\sigma = 0.2$. Two regions highlighted with a white dotted line demonstrate the region where there is a change of amplitude with respect to radial distance (r). r_c is the perpendicular distance from the periphery of the spiral arm towards the inner side. How the r increases for a spiral is indicated by the black arrow line. (b) Represents the heatmap for two regions, A and B, on the spiral arms and how their color is changing with r_c. Since the color of the heatmap is not equivalent, it indicates that there is a change of the spiral's amplitude with respect to r.

In the following stage, we wish to numerically test the analytical prediction for obtaining a spiral for those $\varepsilon\mu_1$ values that satisfy eqn (22). To achieve this, we first present the theoretical $\varepsilon\mu_1$ values for various σ values (which are associated with the source densities of the inhibitor and activator concentrations). In Fig. 4, we provide the corresponding diagram in the $\varepsilon\mu_1$ vs. σ parameter space with a solid curve. To obtain spiral wave patterns, μ is suitably adjusted numerically as the σ value is varied. By subtracting μ_0 from μ (numerical), the numerical values of $\varepsilon\mu_1$ are determined. For various values of σ, these are represented by the triangular points in Fig. 4. This diagram
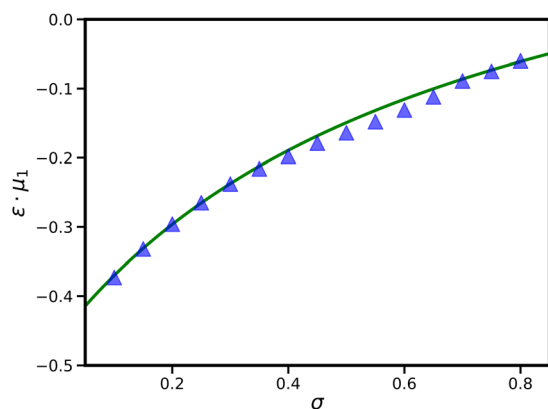

Fig. 4 Bifurcation curves of analytical prediction and numerical simulations in the $\varepsilon\mu_1$ vs. σ parameter space. Other parameter is $D = 0.25$. The green solid line represents the prediction obtained from analytical analysis. Blue triangle points depict the points where numerically spirals have been observed. The diagram shows a well-matching between the analytical predictions and numerical simulations.
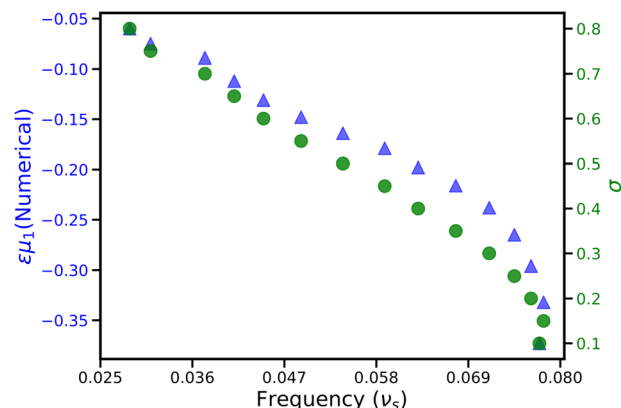

Fig. 5 Numerically estimated frequency (ν_s) values for different spirals perceived for various combinations of $\varepsilon\mu_1$ and σ values. The blue triangle points depict how the frequency values are changing with respect to the numerically calculated $\varepsilon\mu_1$, whereas the green circular points represent how the frequency is varying with respect to the σ values.

clearly demonstrates that the predictions derived from analytical calculations align well with our numerical simulations. Furthermore, we have computed numerically the frequency (ν_s) of the spiral obtained for various σ and $\varepsilon\mu_1$ combinations. It is worth noting that we observed a nearly linear decrease in frequency values with respect to both σ and $\varepsilon\mu_1$. The dependence of frequency values on $\varepsilon\mu_1$ further corroborates our analytical claim in eqn (21). Fig. 5 displays the associated diagram. Blue triangular points in the curve indicate the dependence of frequency values on $\varepsilon\mu_1$, whereas green circular points in the curve indicate the dependence of frequency values on σ.

Now, we aim to analyze the influence of domain size, grid spacing, and boundary conditions, which are critical characteristics for maintaining spiral waves, as highlighted in a previous study.[8]

4.1 Effect of system size, spatial grid length and boundary condition

We first investigate the impact of box size while maintaining a fixed grid spacing. Numerical simulations reveal that increasing the box length from 200 to 800 significantly affects the formed spiral, even with the same grid spacing ($\delta_x = \delta_y = 1.0$). With a larger box length, numerous spiral sources emerge, some rotating counterclockwise and others clockwise. Furthermore, neighboring spirals continuously annihilate each other and form new ones. Notably, for a box size of 300 (Movie 2 in SM), all spiral sources rotate counterclockwise. However, for larger boxes ($L = 400, 800$), both clockwise and counterclockwise rotating spirals appear (Movie 3 and Movie 4 in SM). The corresponding spatial patterns are shown in Fig. 6, where it is evident that with a box size of 300, four spiral sources emerge [Fig. 6(a)], whereas for a box size of 800, the number of spiral sources increases significantly [Fig. 6(c)].

Next, keeping the box length ($L_x = L_y = 200$) fixed, we vary the grid spacing ($\delta_x = \delta_y$) for the numerical simulations. We find
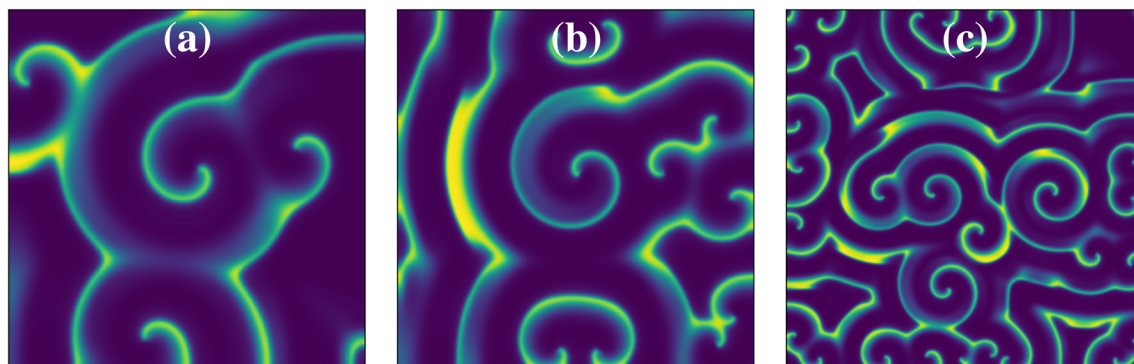
Fig. 6 Effect of box size on the formations of the spiral patterns for a fixed grid spacing ($\delta_x = \delta_y = 1.0$): numerically simulated concentrated profile for activator u for box size-(a) $L_x = L_y = 300$, (b) $L_x = L_y = 400$, and (c) $L_x = L_y = 800$. Other parameter values are $D = 0.25$, $\mu = 0.37$, and $\sigma = 0.2$. With increasing box size, multiple spiral sources arise in the system.

that spirals can form even with smaller grid spacings, though in this case, multiple spiral sources appear, similar to the behavior observed with larger box sizes. Additionally, spiral annihilation and formation occur simultaneously. This differs from the case of larger grid spacing ($\delta_x = 1.0$), where the system tends to maintain a single spiral wave. Finally, we applied periodic boundary conditions in our numerical simulations to assess the effect of boundary conditions on spiral waves. The systematic modification of box sizes, grid spacing, and initial random perturbation of the box domain consistently led to the formation of spiral waves. However, in none of the cases did we observe a single spiral wave. Instead, multiple spiral sources, with both clockwise and counterclockwise rotation, always appeared in the system. Remarkably, in all of these instances, the spirals formed consistently exhibited amplitude fluctuations as a function of radial distance (r). These observations strongly support our analytical conclusion that the amplitude of the spiral must change with respect to the radial distance in order for it to grow highlighting a novel and unique aspect of the system's spatiotemporal dynamics.

While our study primarily focuses on theoretical and numerical aspects, we recognize the importance of linking our findings to experimentally realizable systems. Spiral waves have been observed in a variety of reaction–diffusion systems, including the classic Belousov–Zhabotinsky (BZ) reaction, electrochemical deposition processes, and biological systems such as cardiac tissue and cell signaling networks. However, most reported spiral waves in these contexts exhibit nearly constant amplitudes. The amplitude variation we predict could potentially be observed in experimental systems with specific kinetic and diffusion properties and suitable boundary conditions. In particular, electrochemical systems and metal co-deposition processes,[23,52] where diffusion anisotropy, kinetic feedback mechanisms and boundary effects play a crucial role, may provide a suitable testbed for verifying our findings.

5 Concluding remarks

In this work, we have explored the dynamics of spiral waves in the Gierer–Meinhardt (GM) reaction–diffusion model. Despite

extensive studies of this model over the years,[39–44] the numerical observation of spiral wave-like patterns has not been thoroughly investigated. We employed the multiple-scale analysis perturbative technique to analytically establish the possibility of spiral wave formation. Our analytical results indicate that if the amplitude of the spiral varies with the radial distance, the spiral will grow positively. Additionally, we derived a condition that defines the spatial extent within which the spiral pattern can emerge from the Hopf bifurcation zone.

Our comprehensive numerical analysis of the GM reaction–diffusion model corroborates the theoretical predictions. In all numerically simulated spirals, we observed that the amplitude changes with respect to the radial distance (r). Our findings confirm that the observed amplitude variation is not an artifact of numerical discretization or initial conditions. To ensure the robustness of our results, we performed extensive numerical checks by varying the discretization schemes, using different grid sizes, and altering the domain sizes. Additionally, we tested a range of initial conditions and consistently observed the emergence of spiral waves with varying amplitude. These checks validate that the amplitude modulation is an intrinsic feature of the system rather than a numerical anomaly. Intriguingly, the observed spiral consistently exhibited amplitude modulation as a function of r, regardless of the variations in simulation parameters. This phenomenon, to the best of our knowledge, has not been previously documented in any reaction–diffusion system.

This work not only demonstrates the feasibility of generating spiral waves in the GM reaction–diffusion model but also highlights the potential for creating a novel class of spirals with variable amplitude, opening avenues for further exploration in reaction–diffusion systems. The variation of spiral wave amplitudes in reaction–diffusion (RD) systems is a crucial aspect of pattern formation that can have significant implications across multiple scientific domains:

5.1 Nonlinear chemical dynamics

Spiral waves are fundamental structures in RD systems, and their amplitude variations can indicate underlying instabilities,

© 2025 The Author(s). Published by the Royal Society of Chemistry

mode selection, or the influence of external perturbations. Understanding these variations helps refine theoretical models of chemical oscillations and pattern formation, which are essential for predicting and controlling self-organization in synthetic and natural chemical systems.

5.2 Biological morphogenesis

Many biological processes, such as cell signaling, tissue development, and neural activity, involve RD-based mechanisms. Amplitude variations in spiral waves could influence how biochemical signals propagate in systems like calcium waves in cells, cardiac electrical waves, and embryonic development. Recognizing these effects could improve models of morphogenesis and disease states (*e.g.*, cardiac arrhythmias linked to spiral wave instabilities).

5.3 Materials science

In electrochemical and metal co-deposition systems, spiral waves and other RD patterns influence the deposition morphology and material properties. Understanding amplitude variations can provide insights into the control of surface structures, leading to advances in material fabrication techniques, corrosion prevention, and nanoscale patterning. Similarly, in precipitating RD systems, controlling these variations could allow for the design of ordered structures with specific functionalities.

By studying the mechanisms governing amplitude variations in spiral waves, we gain deeper insights into pattern robustness, stability, and the interplay between reaction kinetics and diffusion. This knowledge not only advances fundamental science but also has potential applications in designing controllable self-organizing systems across chemistry, biology, and materials engineering.

Data availability

The data supporting this article have been included as part of the ESI.†

Author contributions

Tarpan Maiti and Achal Jadhav contributed equally to this study.

Conflicts of interest

There are no conflicts to declare.

Acknowledgements

Notes and references

1 I. R. Epstein and J. A. Pojman, *An Introduction to Nonlinear Chemical Dynamics: Oscillations, Waves, Patterns, and Chaos*, Oxford University Press, New York, 1998.

2 M. Cross and H. Greenside, *Pattern Formation and Dynamics in Nonequilibrium Systems*, Cambridge University Press, 2009.

3 A. M. Turing, *Philos. Trans. R. Soc., B*, 1952, **237**, 37–72.

4 M. C. Cross and P. C. Hohenberg, *Rev. Mod. Phys.*, 1993, **65**, 851–1112.

5 V. Castets, E. Dulos, J. Boissonade and P. De Kepper, *Phys. Rev. Lett.*, 1990, **64**, 2953.

6 B. Rudovics, E. Barillot, P. Davies, E. Dulos, J. Boissonade and P. De Kepper, *J. Phys. Chem. A*, 1999, **103**, 1790–1800.

7 I. Berenstein, L. Yang, M. Dolnik, A. M. Zhabotinsky and I. R. Epstein, *Phys. Rev. Lett.*, 2003, **91**, 058302.

8 P. Ghosh, *Phys. Rev. E*, 2019, **100**, 042217.

9 T. Maiti and P. Ghosh, *J. Chem. Phys.*, 2022, **157**, 224907.

10 T. Maiti and P. Ghosh, *J. Chem. Phys.*, 2023, **159**, 174902.

11 A. Zaikin and A. Zhabotinsky, *Nature*, 1970, **225**, 535–537.

12 A. T. Winfree and W. Jahnke, *J. Phys. Chem.*, 1989, **93**, 2823–2832.

13 T. Plesser, S. C. Mueller and B. Hess, *J. Phys. Chem.*, 1990, **94**, 7501–7507.

14 S. Dutta and O. Steinbock, *Phys. Rev. E:Stat., Nonlinear, Soft Matter Phys.*, 2011, **83**, 056213.

15 F. Haudin, J. H. Cartwright, F. Brau and A. De Wit, *Proc. Natl. Acad. Sci. U. S. A.*, 2014, **111**, 17363–17367.

16 I. Berenstein, A. P. Muñuzuri, L. Yang, M. Dolnik, A. M. Zhabotinsky and I. R. Epstein, *Phys. Rev. E:Stat., Nonlinear, Soft Matter Phys.*, 2008, **78**, 025101.

17 S. Nettesheim, A. Von Oertzen, H. Rotermund and G. Ertl, *J. Chem. Phys.*, 1993, **98**, 9977–9985.

18 A. Volford, F. Izsák, M. Ripszám and I. Lagzi, *Langmuir*, 2007, **23**, 961–964.

19 M. R. Tinsley, D. Collison and K. Showalter, *J. Phys. Chem. A*, 2013, **117**, 12719–12725.

20 M. M. Ayass, M. Al-Ghoul and I. Lagzi, *J. Phys. Chem. A*, 2014, **118**, 11678–11682.

21 M. M. Ayass, I. Lagzi and M. Al-Ghoul, *Phys. Chem. Chem. Phys.*, 2015, **17**, 19806–19814.

22 B. Bozzini, D. Lacitignola and I. Sgura, *Math. Biosci. Eng.*, 2010, **7**, 237–258.

23 B. Bozzini, D. Lacitignola, C. Mele and I. Sgura, *Acta Appl. Math.*, 2012, **122**, 53–68.

24 B. Bozzini, D. Lacitignola and I. Sgura, *J. Solid State Electrochem.*, 2013, **17**, 467–479.

25 F. Siegert and C. Weijer, *J. Cell Sci.*, 1989, **93**, 325–335.

26 P. Camacho and J. D. Lechleiter, *Science*, 1993, **260**, 226–229.

27 R. A. Gray and J. Jalife, *Int. J. Bifurc. Chaos Appl. Sci.*, 1996, **6**, 415–435.

28 T. H. Tan, J. Liu, P. W. Miller, M. Tekant, J. Dunkel and N. Fakhri, *Nat. Phys.*, 2020, **16**, 657–662.

29 S. Liu, Y. Li, Y. Wang and Y. Wu, *Nat. Phys.*, 2024, **20**, 1015–1021.

30 O. Steinbock, V. Zykov and S. C. Müller, *Nature*, 1993, **366**, 322–324.

31 Y. Gong and D. J. Christini, *Phys. Rev. Lett.*, 2003, **90**, 088302.

32 S. Sen, P. Ghosh, S. S. Riaz and D. S. Ray, *Phys. Rev. E:Stat., Nonlinear, Soft Matter Phys.*, 2009, **80**, 046212.

33 S. Sen, P. Ghosh and D. S. Ray, *Phys. Rev. E:Stat., Nonlinear, Soft Matter Phys.*, 2010, **81**, 056207.

34 H. Hu, X. Li, Z. Fang, X. Fu, L. Ji and Q. Li, *Chem. Phys.*, 2010, **371**, 60–65.

35 J. Yang and A. Garfinkel, *Phys. Rev. E:Stat., Nonlinear, Soft Matter Phys.*, 2003, **68**, 066312.

36 B.-W. Li, Y. He, L.-D. Li, L. Yang and X. Wang, *Commun. Nonlinear Sci. Numer. Simul.*, 2021, **99**, 105830.

37 X. Tang, T. Yang, I. R. Epstein, Y. Liu, Y. Zhao and Q. Gao, *J. Chem. Phys.*, 2014, **141**, 024110.

38 J. Gao and C. Gu, *IEEE Access*, 2019, **7**, 140391–140401.

39 A. Gierer and H. Meinhardt, *Kybernetik*, 1972, **12**, 30–39.

40 A.-J. Koch and H. Meinhardt, *Rev. Mod. Phys.*, 1994, **66**, 1481.

41 Y. Song, R. Yang and G. Sun, *Appl. Math. Model.*, 2017, **46**, 476–491.

42 G.-Q. Sun, C.-H. Wang and Z.-Y. Wu, *Nonlinear Dyn.*, 2017, **88**, 1385–1396.

43 L. Guo, X. Shi and J. Cao, *Nonlinear Dyn.*, 2021, **105**, 899–909.

44 S. Ghosh, S. Paul and D. S. Ray, *Phys. Rev. E*, 2016, **94**, 042223.

45 A. Bhattacharyay, *Phys. Rev. E:Stat., Nonlinear, Soft Matter Phys.*, 2001, **64**, 016113.

46 S. S. Riaz and D. S. Ray, *J. Chem. Phys.*, 2005, **123**, 174506.

47 P. Ghosh and D. S. Ray, *J. Chem. Phys.*, 2011, **135**, 104112.

48 M. Banerjee, S. Ghorai and N. Mukherjee, *Int. J. Bifurc. Chaos Appl. Sci.*, 2017, **27**, 1750038.

49 J. Boissonade and P. De Kepper, *J. Phys. Chem.*, 1980, **84**, 501–506.

50 I. Lengyel and I. R. Epstein, *Science*, 1991, **251**, 650–652.

51 R. Yadav, N. Mukherjee and M. Sen, *Nonlinear Dyn.*, 2022, **107**, 1397–1410.

52 B. Bozzini, G. Gambino, D. Lacitignola, S. Lupo, M. Sammartino and I. Sgura, *Comput. Math. Appl.*, 2015, **70**, 1948–1969.

53 S. Koga, *Prog. Theor. Phys.*, 1982, **67**, 164–178.

54 M. Ipsen, L. Kramer and P. G. Sørensen, *Phys. Rep.*, 2000, **337**, 193–235.

55 B. G. Elmegreen, D. M. Elmegreen and P. E. Seiden, *Astrophys. J.*, 1989, **343**, 602–607.

56 B.-W. Li, H. Zhang, H.-P. Ying, W.-Q. Chen and G. Hu, *Phys. Rev. E:Stat., Nonlinear, Soft Matter Phys.*, 2008, **77**, 056207.